High temperature shockwave stabilized single atoms

Yonggang Yao [1,8], Zhennan Huang [2,8], Pengfei Xie [3,8], Lianping Wu [4,8], Lu Ma [5,8], Tangyuan Li [1,8], Zhenqian Pang [4], Miaolun Jiao [1], Zhiqiang Liang [1], Jinlong Gao [1], Yang He [6], Dylan Jacob Kline [7], Michael R. Zachariah [7], Chongmin Wang [6], Jun Lu [5], Tianpin Wu [5*], Teng Li [4*], Chao Wang [3*], Reza Shahbazian-Yassar [2*] and Liangbing Hu [1*]

The stability of single-atom catalysts is critical for their practical applications. Although a high temperature can promote the bond formation between metal atoms and the substrate with an enhanced stability, it often causes atom agglomeration and is incompatible with many temperature-sensitive substrates. Here, we report using controllable high-temperature shockwaves to synthesize and stabilize single atoms at very high temperatures (1,500–2,000 K), achieved by a periodic on–off heating that features a short on state (55 ms) and a ten-times longer off state. The high temperature provides the activation energy for atom dispersion by forming thermodynamically favourable metal–defect bonds and the off-state critically ensures the overall stability, especially for the substrate. The resultant high-temperature single atoms exhibit a superior thermal stability as durable catalysts. The reported shockwave method is facile, ultrafast and universal (for example, Pt, Ru and Co single atoms, and carbon, C_3N_4 and TiO_2 substrates), which opens a general route for single-atom manufacturing that is conventionally challenging.

Single-atom catalysts, which offer a maximized atom-use efficiency and unique coordination environments, are of great interest for catalytic performance enhancements for many reactions, including oxidation[1–3], hydrogenation[4–7], electrocatalysis[8–12] and so on[13–16]. However, the stability of single-atom catalysts remains a great challenge due to the thermodynamically driven atom aggregation, especially at high temperatures[17–21]. In general, atomic dispersions can be achieved by the confinement and coordination of metal atoms to the substrate in wet chemical synthesis to prevent such an aggregation at mild temperatures (<773 K) (refs. [1,4,6,10,22]). Recent studies sought to improve the thermal stability of single atoms by enhancing the metal–substrate absorption[17,23–26] using kinetic or spatial confinement[27–29] or by forming strong metal–substrate bonds by annealing at 800–900 °C (refs. [2,5,8,30,31]). The successful synthesis of single-atom catalysts at higher temperatures naturally grants a higher thermal stability, but high-temperature synthesis (>1,000 °C) is typically challenging to achieve and incompatible with many temperature-sensitive methods and materials.

In this work, we report the use of high-temperature shockwaves to synthesize and stabilize single atoms at very high temperatures (for example, 1,500–2,000 K). The high-temperature shockwave is achieved using a programmable, periodic on–off heating pattern that features a short on state (for example, ~1,500 K for ≤55 ms) and a ten-times longer off state (near room temperature). The on state provides the activation energy for single-atom dispersion by forming thermodynamically stable metal–defect bonds that can naturally sustain high-temperature annealing, which we confirmed with in situ microscopy as well as theoretical simulations. The longer off

state critically ensures the overall dispersion stability by preventing an extended heating-induced metal vaporization and particularly substrate deterioration. The high-temperature-synthesized single atoms (HT-SAs) demonstrate a superior stability in direct methane conversion for 50 hours and are also hydrothermally stable after steam treatment at 973 K.

Shockwave synthesis of thermally stable single atoms. As a demonstration, we began with the synthesis of Pt HT-SAs on CO_2-activated carbon nanofibre (CA-CNF) substrates. As schematically shown in Fig. 1a, ethanol-based salt precursors (H_2PtCl_6) are loaded onto the defective CA-CNFs (loading of 0.01 μmol cm^{-2}, normalized to the geometric area) with good wetting. The precursor-loaded CA-CNF film was then subjected to shockwave heating via an electrical Joule heating process that can be easily programmed in terms of temperature, on–off durations and repeated cycles (Supplementary Fig. 1). The thermal images captured by a high-speed camera show a uniform spatial temperature distribution during the shock-heating process (Supplementary Fig. 2). Figure 1b shows the temperature evolution of a pulse heated to ~1,500 K for 55 ms and then rapidly quenched by directly cutting off the input current for a ten times longer period, which leads to an average temperature of ~400 K for the overall process. Figure 1c shows the temperature profile with ten heating cycles over a 6 s period, which demonstrates the relatively stable temperature that can be repeatedly achieved during the heating process. In addition, we can achieve a temperature of up to ~3,000 K (Supplementary Fig. 2c), which allows us to synthesize thermally stable HT-SAs at very high temperatures.

[1]Department of Materials Science and Engineering, University of Maryland, College Park, MD, USA. [2]Department of Mechanical and Industrial Engineering, University of Illinois at Chicago, Chicago, IL, USA. [3]Department of Chemical and Biomolecular Engineering, Johns Hopkins University, Baltimore, MD, USA. [4]Department of Mechanical Engineering, University of Maryland, College Park, MD, USA. [5]X-ray Science Division and Chemical Sciences and Engineering Division, Argonne National Laboratory, Lemont, IL, USA. [6]Environmental Molecular Sciences Laboratory, Pacific Northwest National Laboratory, Richland, WA, USA. [7]Department of Chemical and Biomolecular Engineering and Chemistry and Biochemistry, University of Maryland, College Park, MD, USA. [8]These authors contributed equally: Yonggang Yao, Zhennan Huang, Pengfei Xie, Lianping Wu, Lu Ma, Tangyuan Li *e-mail: twu@anl.gov; lit@umd.edu; chaowang@jhu.edu; rsyassar@uic.edu; binghu@umd.edu
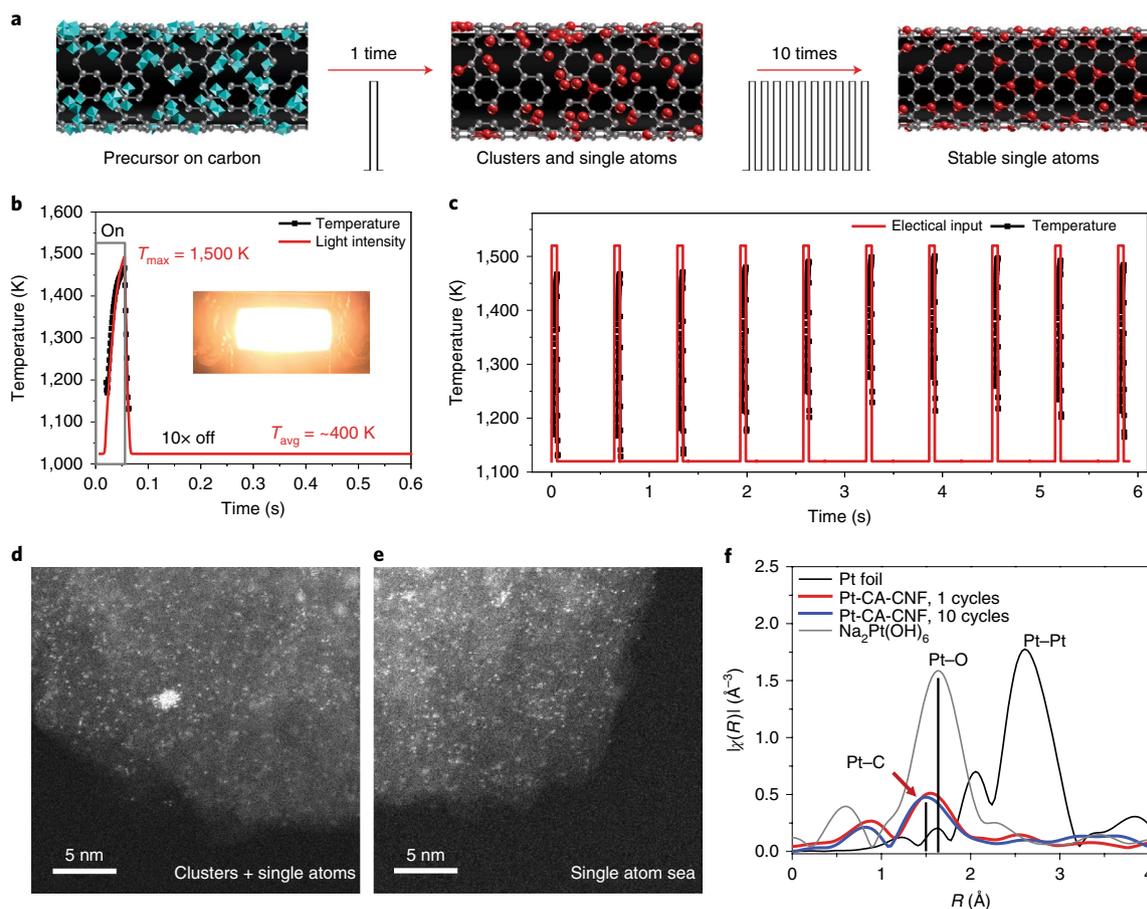
Fig. 1 | In situ high-temperature-shockwave synthesis of HT-SAs on defective carbon. a, The schematic diagram shows the HT-SA synthesis and dispersion process (grey, carbon atoms; cyan, metal precursor; red, metallic atoms). **b**, Temperature evolution during the shockwave synthesis and a detailed heating/cooling pattern. Inset: light emitted from the material at a high temperature. **c**, A ten-pulse shock heating pattern demonstrates the uniform temperature in each cycle with a high-temperature on state and a low temperature off state. **d,e**, Typical HAADF images of Pt HT-SAs after one (**d**) and ten (**e**) cycles of the thermal shock ($0.01\,\mu\mathrm{mol\,cm^{-2}}$). **f**, EXAFS profiles (without phase correction) for Pt HT-SAs on CA-CNFs after one and ten cycles of the thermal shock treatment.

Figure 1d,e shows the high-angle annular dark-field (HAADF) images of Pt dispersed on the CA-CNF substrate after one and ten heat shocks at 1,500 K. For a single heat shock, the surface of the CA-CNFs was dispersed with high-density single atoms, although Pt clusters were also visible (Fig. 1d and Supplementary Fig. 3a). However, after ten shocks, the substrate displayed a mostly uniform single-atom distribution (Fig. 1e and Supplementary Fig. 3b), which indicates the stability of these HT-SAs and the further disassembly of clusters into single atoms during the continuous shockwave heating. We further confirmed the single-atom dispersion by macroscopic extended X-ray absorption fine structure (EXAFS) (Fig. 1f) and X-ray near-edge structure analysis (Supplementary Fig. 3c). The EXAFS spectrum of the one-cycle sample shows a weak peak at ~2.5 Å, which corresponds to the Pt–Pt bonding, and a dominant peak at ~1.5 Å, which indicates the Pt–substrate bonds (the Pt–C bond, as discussed later), to reveal a structure of Pt nanoclusters mixed with single atoms. After ten cycles, nearly no Pt–Pt bonds remained, which suggests the dominance of single-atom dispersion by disassembling the remaining clusters. The CA-CNF substrate had a surface area of ~56 m²g⁻¹ and the Pt loading was measured as ~0.24 wt%. We also varied the metal loading and found that nanoclusters form at a higher (5 times and 10 times) loading (Supplementary Fig. 4 shows the cases of 0.05 and $0.1\,\mu\mathrm{mol\,cm^{-2}}$) owing to limited stabilization sites.

To understand the dispersion mechanism, we designed control samples using different heating strategies (Supplementary Fig. 5a–c). Low-temperature synthesis (573 K, 1 h) lacks the activation energy to effectively disperse and bond these atoms to the substrate (that is, poor dispersion and stability), whereas high-temperature annealing (1,500 K, 10 min) leads to a serious particle agglomeration due to overheating-induced (1) graphitization of the carbon substrate (that is, the losing of defects)[32] and (2) long-range atom diffusion. Therefore, the shockwave heating creatively utilized high temperatures for HT-SAs synthesis but was short enough to avoid the deterioration to the substrates, and thus maintained the stability of the single-atom dispersion.

In addition, the defects are important to help bind these mobile single atoms onto the substrate and improve their structural stability (Supplementary Fig. 5d–f). Experimentally, shockwave synthesis on the relatively crystalline CNF (without CO_2 activation) yields nanoclusters mixed with single atoms due to the limited defective sites. In contrast, after activation, the improved defect concentration and presence of micropores (that is, carbon vacancies) on CA-CNFs (Supplementary Figs. 6 and 7) lead to a high-density single-atom dispersion. Accordingly, a more defective substrate can accommodate a high density of single atoms. Therefore, these control experiments illustrate the critical role of high-temperature shockwave heating and of
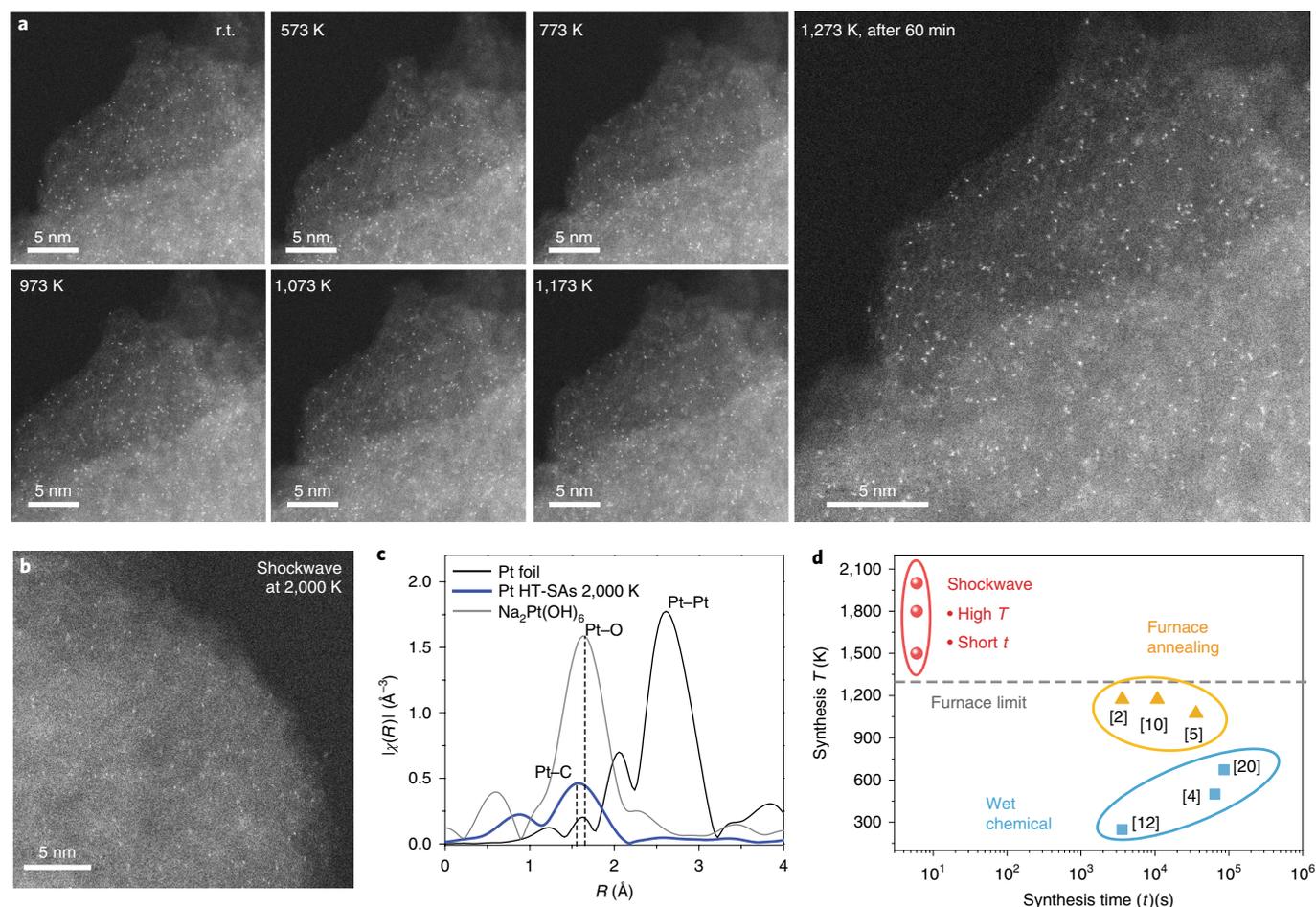
Fig. 2 | Thermal stability of the HT-SAs. a, We evaluated the morphology of Pt HT-SAs on the CA-CNF substrate using in situ STEM from room temperature up to 1,273 K, which demonstrated the superior thermal stability. **b,c**, A higher-temperature shockwave synthesis at 2,000 K (loading of 0.005 µmol cm⁻²) also produced thermally stable HT-SAs (**b**), as shown by its corresponding EXAFS profiles (without phase correction) (**c**). **d**, Summary of the results of single-atom synthesis temperatures and time by our shockwave method and other techniques in the literature (square brackets)[2,4,5,10,12,20]. r.t., room temperature.

defects on the substrate for an effective single-atom dispersion and stabilization.

The HT-SAs naturally possess a superior structural stability because they were synthesized at a high temperature of 1,500 K, which we confirmed by in situ scanning transmission electron microscopy (STEM) from room temperature up to 1,273 K (the equipment limit). The sample was stabilized for at least 30 minutes before taking images. As shown in Fig. 2a, the Pt HT-SAs displayed a uniform and high-density single-atom dispersion at each temperature up to 1,273 K after holding for 60 minutes. In addition, we also confirmed the stability of the Pt HT-SAs by performing ex situ thermal annealing at 1,073 K for 1 hour in a furnace with an Ar flow (Supplementary Fig. 8). As the shockwave method can produce a temperature of up to 3,000 K (Supplementary Fig. 2c)[33], this could enable the synthesis of HT-SAs at an even higher temperature. As an example, we synthesized HT-SAs at 1,800 and 2,000 K (using a lower (half) loading of 0.005 µmol cm⁻²) and observed the stable single-atom dispersion proved by both STEM and EXAFS measurements (Fig. 2c and Supplementary Fig. 9).

For comparison, in Fig. 2d we summarize previous reports of single atoms synthesized using various methods. Most wet chemical approaches use a mild temperature (<773 K) and the resulting single atoms are vulnerable under subsequent high-temperature annealing, especially when there is no proper bonding or coordination

with the substrate[17,19,27,28]. Furnace heating or annealing at 1,073–1,173 K can substantially increase the thermal stability of single atoms by creating strong and stable metal–substrate bonding through atom trapping and substrate anchoring[2,5,8,30]. However, the much higher temperature of our shockwave method surpasses furnace heating with the ability to synthesize single atoms up to 1,500–2,000 K. In addition, a higher-temperature synthesis provides ultrafast kinetics for single-atom dispersion with extremely shorter processing durations (<10 s) and a higher efficiency compared to low-temperature methods.

Analysis of the single-atom bond structure. The thermal stability of HT-SAs comes from the Pt–substrate bond's ability to resist high-temperature annealing. Experimentally, we analysed the bond structure by extracting the nearest-neighbour coordination numbers and the local structure of the Pt HT-SAs from fitting the EXAFS profiles with first-shell model (Table 1 and Supplementary Fig. 10). Figure 3a shows a typical EXAFS fitting of Pt 1,500 K HT-SAs, which renders a bond distance of 1.931 Å and a coordination number of 2.8 (indicating a Pt–X₃ bond configuration). The experimentally derived bond length is considerably shorter than the literature reported Pt–O (2.01–2.05 Å) (refs. [10,34]) and Pt–N bonds (~2.3 Å) (ref. [35]), but it is in good agreement with a Pt–C bond that has a calculated bond length of 1.93 Å (ref. [36]). Moreover, based on

Table 1 | Fitting parameters of the Fourier transform of the first shell of the EXAFS spectra

Sample	Scatter	CN	R (Å)	σ^2 (Å^2)	E_0 (eV)
Pt 1,500 K 1 cycle	Pt–C	2.46 ± 0.62	1.941 ± 0.027	0.0063 ± 0.0038	3.40
Pt 1,500 K 10 cycles	Pt–C	2.81 ± 0.70	1.931 ± 0.027	0.0075 ± 0.0037	−0.09
Pt HT-SAs 2,000 K	Pt–C	2.85 ± 0.65	1.950 ± 0.026	0.0084 ± 0.0038	4.15
Pt–O (ref. [34])	Pt–O	6	2.017		
Pt–N (ref. [35])	Pt–N	4	2.309		
Pt–C$_3$ (DFT)	Pt–C	3	1.940		
Pt–N$_3$ (DFT)	Pt–N	3	2.188		
Pt–O$_2$C$_2$ (DFT)	Pt–O	2	2.052		

CN, coordination number; R, bond distance, σ^2, Debye–Waller factor; E_0, edge energy shift (R-factor ≤0.009).

this Pt–X$_3$ bond model, we calculated the bond distance of Pt–C in Pt–C$_3$, Pt–N in Pt–N$_3$ and Pt–O in Pt–O$_2$C$_2$ using density functional theory (DFT)[37–40]. The calculated Pt–C bond in the Pt–C$_3$ configuration shows a bond distance of 1.940 Å, which is very close to the experimentally fitted result, whereas the Pt–N and Pt–O bonds all have much larger bond distances (Fig. 3b), which confirms the Pt–C bond structure in our samples.

The DFT result also reveals that the bonding energy of Pt–C bonds is surprisingly higher than that of Pt–N bonds under the similar bond configurations (Pt–X$_3$ and Pt–X$_4$) (Supplementary Fig. 11a). In addition, the charge density difference diagrams further illustrate the difference between Pt–C and Pt–N bonds: in Pt–C bonds, a large amount of charge transfer appears between the Pt and C atoms and the charge density is mainly concentrated in the centre, which indicates a strong covalent bond nature; however, in Pt–N bonds, the transferred electron is mainly circulated around the Pt and N atoms, which denotes an ionic bond (Supplementary Fig. 11b). Therefore, the Pt–C bonds demonstrate a higher binding energy and a unique covalent nature compared with Pt–N bonds in a similar bond configuration.

High-temperature dispersion and stabilization. To understand the atomistic origin of the high-temperature-induced dispersion and stabilization, we performed molecular dynamic (MD) simulations using the reactive force field (ReaxFF) potential[41,42] (details in Supplementary Methods). The defects on graphene contain randomly etched carbon vacancies to mimic the surface of CA-CNFs. Figure 3c clearly depicts the dispersion of Pt clusters into single atoms with increasing heating cycles at 1,500 K (from (i) to (iii)), as well as the dispersion stability on thermal annealing at 1,500 K (iv). We observed both the agglomeration and atomization of Pt atoms, but the atomization can only be stabilized when energy-favourable Pt–C bonds are formed (types 4–10 in Fig. 3d). Figure 3e shows the evolution of bond structures before and after a shockwave at 1,500 K, in which all the initial weak bonds (Pt–Pt cluster and types 1–3 Pt–C bonds) change into stronger Pt–C bonds (types 4–10) with higher binding energies, which illustrates the atomic origin as to why the HT-SAs are more thermally stable than Pt clusters. The simulation clearly reproduced our synthesis process in which the initial Pt clusters are weakly attached with the substrate, but with more shockwave heating, the clusters are disassembled into single atoms by forming thermodynamically stable Pt–C bonds that can sustain high-temperature annealing. This also indicates defects on the substrates are essential to stabilize HT-SAs and determine the dispersion density.

In the process, high temperature is critical to provide sufficient activation energy for atom diffusion and overcome the energy barrier for bond formation. As an example, when a single Pt atom deviates from a Pt-30 cluster to form a Pt–C bond, kinetically there is an energy barrier (for example, 1.48 eV) that hinders the dispersion, which can only be overcome at a high temperature (Fig. 3f and Supplementary Fig. 12). We also simulated the shockwave dispersion at other temperatures: 500, 1,000, 2,000 and 2,500 K (Supplementary Fig. 13). Although similar shockwave patterns (on/off ratio and cycle numbers) were applied, low temperatures (500 and 1,000 K) failed to fully disperse the Pt cluster within the given repeated cycles. In contrast, higher shockwave temperatures had improved kinetics and achieved single-atom dispersion much faster, that is, gave a much higher dispersion efficiency (Fig. 3g). Moreover, the Pt–C bond distribution in these HT-SAs shows an increasing proportion of more stable type 5–10 bonds at higher synthesis temperatures, which indicates an improved thermal stability (Fig. 3h). Therefore, high-temperature synthesis is critical for single-atom dispersion and stabilization as it provides the essential activation energy to accelerate the dispersion process and promote the formation of bonds that are more stable.

Generality of the shockwave synthesis and catalytic study. The simple shockwave synthesis method can generally be applied to other metals and substrates in which a high temperature enables the atom dispersion by forming stable metal–defect bonds while the shockwave heating helps maintain the overall stability. As the shockwave temperature is sufficiently high compared with the thermal decomposition temperatures of most metal precursors, our method can be used to produce single-atom dispersions of most metals, as demonstrated of Ru and Co HT-SAs on CA-CNFs (Fig. 4a and Supplementary Fig. 14).

In addition, the shockwave method can be extended to other substrates, such as conductive reduced graphene oxide, semiconductor C$_3$N$_4$ and oxides like TiO$_2$, but with a different heating method (Supplementary Fig. 15) and forming different bonds with the substrates (Supplementary Fig. 16). Radiative shockwave heating can be used for powder samples by depositing precursor-loaded powders beneath a carbon film that was Joule heated in a shockwave pattern. The high temperature achieved in the film also heated the C$_3$N$_4$ powder and induced a high-density single-atom dispersion (Fig. 4b). In addition, the shockwave heating maintained the structural integrity of C$_3$N$_4$, which otherwise would be easily carbonized by prolonged heating (Supplementary Fig. 17). The non-contact radiative heating can also be scaled up easily for a continuous production (Supplementary Fig. 18). Alternatively, as oxides have a poor thermal conductivity for effectively radiative heating, we achieved Pt HT-SAs on TiO$_2$ substrates by depositing a thin layer (~2.5 nm) of TiO$_2$ on the nanofibres in a CA-CNF film via atomic layer deposition (Supplementary Fig. 15c). The shockwave heating of the CA-CNF film also heated the TiO$_2$ layer through conductive heating and induced the single-atom dispersion on TiO$_2$ (Fig. 4c). These results demonstrate the generality of the
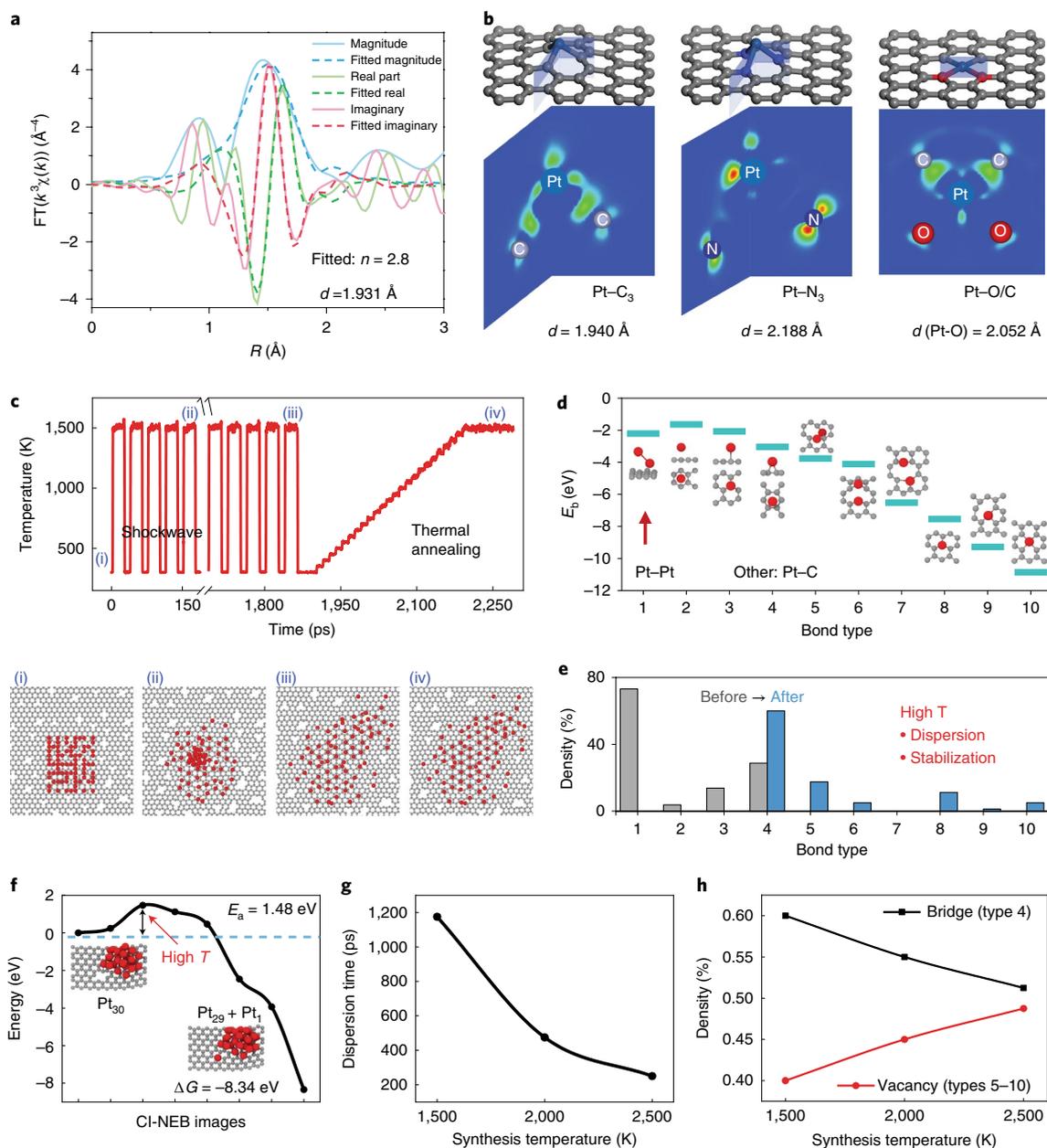
Fig. 3 | HT-SA dispersion mechanism and temperature effect a, The first-shell model EXAFS fitting of the Fourier transform (FT) at the Pt L_3 edge for the Pt 1,500 K 10 cycles sample shows a bond distance of 1.931 Å with a coordination number of 2.8. **b**, DFT-calculated bond distances in the Pt–C_3, Pt–N_3 and Pt–O_2C_2 configurations. **c**, MD simulation on the single-atom dispersion ((i)–(iii)) and subsequent annealing (iv) at 1,500 K. **d**, Identified Pt–Pt (type 1) and Pt–C bonds (types 2–10) in the dispersion system. **e**, The statistical distribution of bond configurations before (i) and after (iii) the shockwave synthesis at a high temperature in **c**—the weak bonds become strong Pt–C bonds. **f**, Energy analysis of a Pt atom deviated from a Pt-30 cluster by forming a thermodynamically stable Pt–C bond (type 10). **g,h**, Time needed for single-atom dispersion (**g**) and associated bond configuration at different synthesis temperatures (**h**). The high temperature provides the activation energy for the bond formation to give a higher dispersion efficiency (**g**) with more stable Pt–C bonds (types 5–10) at higher synthesis temperatures (**h**). CINEB, climbing image-nudged elastic band.

high-temperature-shockwave method for synthesizing thermally stable single-atom dispersions, which suggests a great potential for scalable nanomanufacturing.

To test the stability of our HT-SAs, we first performed an in situ hydrothermal test for Pt HT-SAs on CA-CNFs in an environmental TEM (ETEM) at a partial H_2O pressure of 10^{-3} mbar from 300 to 773 K (the upper limit is to avoid equipment corrosion), with each studied temperature held for at least 30 minutes. As shown in Supplementary Fig. 19, no nanocluster emerged during the in situ measurement up to 773 K, which proves the HT-SAs are stable. We further confirmed the performance stability of the Pt HT-SAs in the CO oxidation reac-

tion before and after hydrothermal treatment using 5% H_2O at 973 K for four hours, which corroborates the hydrothermal stability of the Pt HT-SAs (Fig. 4d). The Arrhenius plots measured by kinetic studies (Fig. 4e) also show that the apparent reaction energies of the Pt single-atom catalysts before and after the steam pretreatment are very close (50.7 kJ mol^{-1} versus 53.2 kJ mol^{-1}). In addition, we performed multiple cycles of the CO oxidation measurements (Supplementary Fig. 20), as well as a stability test at 493 K for 50 hours, and both confirmed the high stability of the Pt HT-SAs (Fig. 4f).

Additionally, we demonstrated that the HT-SAs have a reductive catalytic application in direct methane conversion, in which
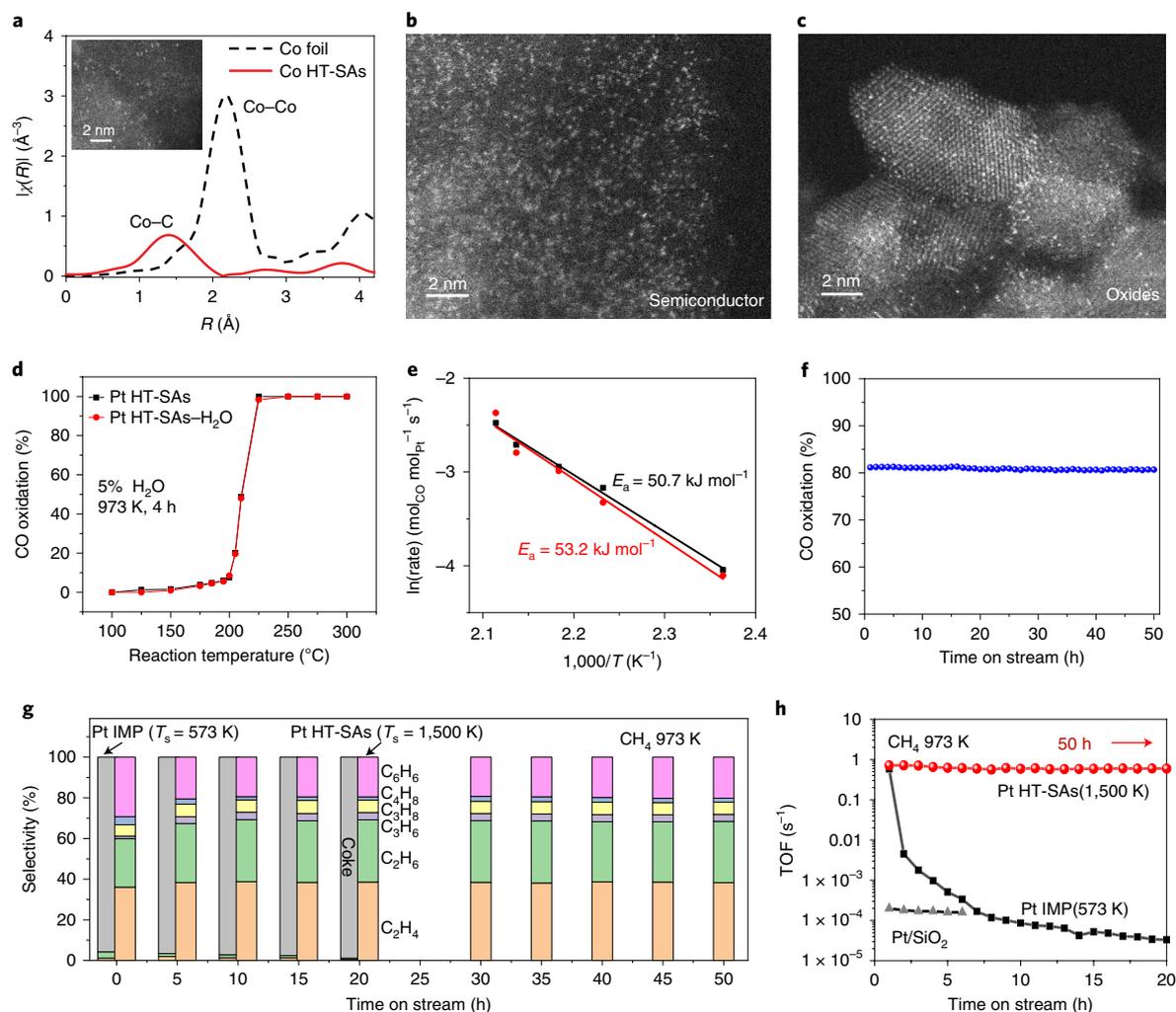
Fig. 4 | The generality of the shockwave method and HT-SAs in catalytic reactions. a, Co HT-SAs synthesized on CA-CNFs confirmed by the EXAFS profile and a HAADF image (inset). **b,c**, Pt HT-SAs synthesized on C_3N_4 (**b**) and TiO_2 (**c**) substrates through radiative and conductive shockwave synthesis (~0.5 wt%). **d,e**, The light-off curves (**d**) and the Arrhenius plots (**e**) of the Pt HT-SAs for the CO oxidation reaction before and after steam treatment at 973 K for 4 h show a stable performance after hydrothermal treatment. **f**, The stable performance of the Pt HT-SAs during CO oxidation at 493 K for 50 h. **g**, High-temperature direct CH_4 conversion at 973 K by Pt HT-SAs for 50 h and Pt IMP samples for 20 h. **h**, The reaction TOF compared with the literature value for nanocluster Pt/SiO_2 (ref. [43]).

single-atom catalysts exhibit good performances due to the coke resistance by preventing catalytic C–C coupling[43,44]. A control sample was synthesized via a conventional impregnation (that is, IMP) method by using the same material but thermally reducing it at 573 K for one hour (Supplementary Fig. 21). Figure 4g and Supplementary Fig. 22 display the performance of Pt IMP and Pt HT-SAs for the direct CH_4 conversion at 973 K to give various products, such as ethylene, ethane, propylene, propane, butene and benzene among others. The product distribution shows a high selectivity for C_2H_4, C_2H_6 and C_6H_6 (>90%) for Pt HT-SAs and no coke formation for extended 50 h. In contrast, the Pt IMP sample shows severe coke formation even during the first hour of reaction, which could be ascribed to the continuous ensembles and aggregation of Pt sites at a high temperature (973 K). Figure 4h shows the superior stability of the Pt HT-SAs in CH_4 conversion with a stable turnover frequency (TOF) for 50 h, in contrast to the quick drop of TOF for the Pt IMP sample due to its dispersion instability at a high temperature and aggregation into nanoclusters. Note that our HT-SAs demonstrate a roughly 1,000-times higher TOF than the Pt nanocluster supported on SiO_2 catalysts reported in the literature under simi-

lar conditions[43], which manifests the criticalness and great efficiency of single-atom catalysts. These practical results demonstrate the superior thermal stabilities of HT-SAs synthesized by high-temperature shockwaves and their great potential for catalytic applications.

Conclusion

We report a high-temperature-shockwave method to synthesize and stabilize high-density single atoms at very high temperatures with a great efficiency. The shockwave design enables a high-temperature (1,500–2,000 K) synthesis during the on state; however, the average temperature is significantly lower (for example, 400 K) as a result of the extended off times, which makes the method compatible with various substrates and manufacturing. Control experiments and simulation results revealed the critical roles of high-temperature synthesis, which provides the activation energy and ultrafast kinetics for single-atom dispersion and promotes a more-stable bond formation with the defects on the substrates. We confirmed the high-temperature stability of the HT-SAs by in situ (stable up to 1,273 K) and ex situ STEM (shockwave stability up to 1,500–2,000 K). We also demonstrated the stability of HT-SAs in CO oxidation and in direct

methane conversion over 50 hours. The shockwave method is facile and general for synthesizing various thermally stable single atoms on different substrates, which provides a route for single-atom manufacturing to give high-temperature catalytic reactions.

Online content

Any methods, additional references, Nature Research reporting summaries, source data, statements of code and data availability and associated accession codes are available at https://doi.org/10.1038/s41565-019-0518-7.

References

1. Qiao, B. et al. Single-atom catalysis of CO oxidation using Pt_1/FeO_x. *Nat. Chem.* **3**, 634–641 (2011).
2. Jones, J. et al. Thermally stable single-atom platinum-on-ceria catalysts via atom trapping. *Science* **353**, 150–154 (2016).
3. Nie, L. et al. Activation of surface lattice oxygen in single-atom Pt/CeO_2 for low-temperature CO oxidation. *Science* **358**, 1419–1423 (2017).
4. Li, H. et al. Synergetic interaction between neighbouring platinum monomers in CO_2 hydrogenation. *Nat. Nanotechnol.* **13**, 411–417 (2018).
5. Wei, S. et al. Direct observation of noble metal nanoparticles transforming to thermally stable single atoms. *Nat. Nanotechnol.* **13**, 856–861 (2018).
6. Liu, P. et al. Photochemical route for synthesizing atomically dispersed palladium catalysts. *Science* **352**, 797–800 (2016).
7. Lucci, F. R. et al. Selective hydrogenation of 1,3-butadiene on platinum–copper alloys at the single-atom limit. *Nat. Commun.* **6**, 8550 (2015).
8. Fei, H. et al. General synthesis and definitive structural identification of MN_4C_4 single-atom catalysts with tunable electrocatalytic activities. *Nat. Catal.* **1**, 63–72 (2018).
9. Tiwari, J. N. et al. Multicomponent electrocatalyst with ultralow Pt loading and high hydrogen evolution activity. *Nat. Energy* **3**, 773–782 (2018).
10. Wei, H. et al. Iced photochemical reduction to synthesize atomically dispersed metals by suppressing nanocrystal growth. *Nat. Commun.* **8**, 1490 (2017).
11. Duchesne, P. N. et al. Golden single-atomic-site platinum electrocatalysts. *Nat. Mater.* **17**, 1033–1039 (2018).
12. Yang, H. Bin et al. Atomically dispersed Ni(I) as the active site for electrochemical CO_2 reduction. *Nat. Energy* **3**, 140–147 (2018).
13. Qin, R., Liu, P., Fu, G. & Zheng, N. Strategies for stabilizing atomically dispersed metal catalysts. *Small Methods* **2**, 1700286 (2018).
14. Chen, Y. et al. Single-atom catalysts: synthetic strategies and electrochemical applications. *Joule* **2**, 1242–1264 (2018).
15. Liu, J. Catalysis by supported single metal atoms. *ACS Catal.* **7**, 34–59 (2017).
16. Pelletier, J. D. A. & Basset, J. M. Catalysis by design: well-defined single-site heterogeneous catalysts. *Acc. Chem. Res.* **49**, 664–677 (2016).
17. Zhang, Z. et al. Thermally stable single atom $Pt/m-Al_2O_3$ for selective hydrogenation and CO oxidation. *Nat. Commun.* **8**, 16100 (2017).
18. Hansen, T. W., Delariva, A. T., Challa, S. R. & Datye, A. K. Sintering of catalytic nanoparticles: particle migration or Ostwald ripening? *Acc. Chem. Res.* **46**, 1720–1730 (2013).
19. Risse, T., Shaikhutdinov, S., Nilius, N., Sterrer, M. & Freund, H. J. Gold supported on thin oxide films: from single atoms to nanoparticles. *Acc. Chem. Res.* **41**, 949–956 (2008).
20. Kim, Y. T. et al. Fine size control of platinum on carbon nanotubes: from single atoms to clusters. *Angew. Chem. Int. Ed.* **45**, 407–411 (2006).
21. Sehested, J., Gelten, J. A. P., Remediakis, I. N., Bengaard, H. & Nørskov, J. K. Sintering of nickel steam-reforming catalysts: effects of temperature and steam and hydrogen pressures. *J. Catal.* **223**, 432–443 (2004).
22. Li, X. et al. Single-atom Pt as Co-catalyst for enhanced photocatalytic H_2 evolution. *Adv. Mater.* **28**, 2427–2431 (2016).
23. Kwak, J. H. et al. Coordinatively unsaturated Al^{3+} centers as binding sites for active catalyst phases of platinum on $γ-Al_2O_3$. *Science* **325**, 1670–1673 (2009).
24. Choi, C. H. et al. Tuning selectivity of electrochemical reactions by atomically dispersed platinum catalyst. *Nat. Commun.* **7**, 10922 (2016).
25. Dvořák, F. et al. Creating single-atom Pt–ceria catalysts by surface step decoration. *Nat. Commun.* **7**, 10801 (2016).
26. Qiu, H. J. et al. Nanoporous graphene with single-atom nickel dopants: an efficient and stable catalyst for electrochemical hydrogen production. *Angew. Chem. Int. Ed.* **54**, 14031–14035 (2015).
27. Liu, L. et al. Generation of subnanometric platinum with high stability during transformation of a 2D zeolite into 3D. *Nat. Mater.* **16**, 132–138 (2017).
28. Moliner, M. et al. Reversible transformation of Pt nanoparticles into single atoms inside high-silica chabazite zeolite. *J. Am. Chem. Soc.* **138**, 15743–15750 (2016).
29. Li, Z. et al. Platinum–nickel frame within metal–organic framework fabricated in situ for hydrogen enrichment and molecular sieving. *Nat. Commun.* **6**, 1–8 (2015).
30. Yin, P. et al. Single cobalt atoms with precise N-coordination as superior oxygen reduction reaction catalysts. *Angew. Chem. Int. Ed.* **55**, 10800–10805 (2016).
31. Xie, P. et al. Nanoceria-supported single-atom platinum catalysts for direct methane conversion. *ACS Catal.* **8**, 4044–4048 (2018).
32. Yao, Y. et al. Carbon welding by ultrafast Joule heating. *Nano Lett.* **16**, 7282–7289 (2016).
33. Yao, Y. et al. Carbothermal shock synthesis of high-entropy-alloy nanoparticles. *Science* **359**, 1489–1494 (2018).
34. Bugaris, D. E., Smith, M. D. & Zur Loye, H. C. Hydroflux crystal growth of platinum group metal hydroxides: $Sr_6NaPd_2(OH)_{17}$, $Li_2Pt(OH)_6$, $Na_2Pt(OH)_6$, $Sr_2Pt(OH)_8$, and $Ba_2Pt(OH)_8$. *Inorg. Chem.* **52**, 3836–3844 (2013).
35. Cheng, N. et al. Platinum single-atom and cluster catalysis of the hydrogen evolution reaction. *Nat. Commun.* **7**, 13638 (2016).
36. Sun, X., Han, P., Li, B. & Zhao, Z. Tunable catalytic performance of single Pt atom on doped graphene in direct dehydrogenation of propane by rational doping: a density functional theory study. *J. Phys. Chem. C* **122**, 1570–1576 (2018).
37. Monkhorst, H. J. & Pack, J. D. Special points for Brillouin-zone integrations. *Phys. Rev. B* **13**, 5188–5192 (1976).
38. Kresse, G. & Hafner, J. Ab initio molecular dynamics for liquid metals. *Phys. Rev. B* **47**, 558 (1993).
39. Perdew, J. P., Burke, K. & Ernzerhof, M. Generalized gradient approximation made simple. *Phys. Rev. Lett.* **77**, 3865–3868 (1996).
40. Kresse, G. & Furthmüller, J. Efficient iterative schemes for ab initio total-energy calculations using a plane-wave basis set. *Phys. Rev. B* **54**, 11169–11186 (1996).
41. Sanz-Navarro, C. F. et al. Molecular dynamics simulations of the interactions between platinum clusters and carbon platelets. *J. Phys. Chem. A* **112**, 1392–1402 (2008).
42. Plimpton, S. Fast parallel algorithms for short-range molecular dynamics. *J. Comput. Phys.* **117**, 1–19 (1995).
43. Gerceker, D. et al. Methane conversion to ethylene and aromatics on PtSn catalysts. *ACS Catal.* **7**, 2088–2100 (2017).
44. Guo, X. et al. Direct, nonoxidative conversion of methane to ethylene, aromatics, and hydrogen. *Science* **344**, 616–619 (2014).

Author contributions

L.H. and Y.Y. contributed to the idea and experimental design. Y.Y., T.L., M.J. and Z.L. conducted the experiments and materials preparation. Z.H. and R.S.-Y. performed the high-resolution microscopy. P.X. and Chao Wang contributed to the catalysis evaluation. L.W., Z.P. and T.L. conducted the simulation analysis. L.M., T.W. and J.L. contributed to the X-ray absorption measurements and analysis. Y.H. and Chongmin Wang performed the in situ environmental microscopy. D.J.K. and M.R.Z. performed the temperature characterization and thermal gravimetric analysis. L.H. and Y.Y. wrote the paper and all the authors commented on the final manuscript.

Methods

Materials and substrates. All the salt precursors, H_2PtCl_6 hydrate (99.995%), $RuCl_3 \cdot xH_2O$ (>98%) and $CoCl_2 \cdot 6H_2O$ (98%), were purchased from Sigma-Aldrich without further purification. CNF substrates were derived from polyacrylonitrile (Sigma-Aldrich) by electrospinning an 8 wt% polyacrylonitrile in dimethylformamide (Sigma-Aldrich) solution at a voltage of 15–20 kV, a spinning distance of 10 cm and a feed rate of 1 ml h^{-1}. The nanofibre mat was first stabilized in air at 533 K for 5 h and carbonized at 1,273 K for 2 h in Ar to create the CNF sample. The CNF material was then thermally annealed under a CO_2 atmosphere (80 ml min^{-1}) at 1,023 K for 3 h (CA-CNF). Reduced graphene oxide was synthesized according to a modified Hummer's method[45] and then thermally reduced at 300 °C for 2 h in an Ar-protected tube furnace. The C_3N_4 powder substrate was synthesized by pyrolysis of melamine powder at 550 °C for 2 h in a muffle furnace. The TiO_2-coated CA-CNFs were fabricated using atomic layer deposition (Beneq TFS 500 ALD) of alternating a Ti precursor and H_2O for 50 cycles (estimated TiO_2 thickness of 2.5 nm).

Shockwave synthesis. The salt precursors were dissolved in ethanol-based solutions at a dilute concentration (0.0001–0.0005 mol l^{-1}), and the solutions were directly dropped onto the suspended CNF films with a loading of 20–100 μLcm^{-2} (in total ~0.01 μmol cm^{-2}) and left to dry (room temperature, 30 min). The precursor-loaded CNF films were then subjected to the shockwave synthesis in an Ar-filled glovebox using a programmable electrical pulse (Keithley 2425). The pulse temperature, duration and on–off ratio were easily adjusted by the programming in the Keithley 2425 system (the sweep function) or by an external control software. A high-power d.c. source (Volteq, 1,200 W) was also used when a high input power was needed. The programmable pulse heating o the high-power electric source was controlled by Keithely through a relay.

To estimate the temperature evolution during the shockwave process, a homemade colour ratio pyrometer measurement was performed using a Vision Research Phantom Miro M110 high-speed camera. Detailed temperature calculations are given in a previous paper[46]. MATLAB was used to extract the raw pixel values to calculate the temperatures. For the figures that show the temperature of a single sample as a function of time, only unsaturated pixels above the black level and within the error threshold were used to report the mean and median temperature of the frame for a contiguous area of at least ten acceptable pixels.

Characterizations. The microstructure was characterized by SEM (Hitachi SU-70 FEG-SEM at 10 kV) and TEM (JEOL 2100F FEG TEM and JEOL TEM/STEM ARM 200CF equipped with HAADF and annular bright-field detectors). The HAADF images were acquired using the JEOL ARM 200CF with a 90 mrad inner-detector angle. The in situ TEM thermal stability study was performed using a Protochips Fusing holder with the sample loading on the corresponding heating E-Chip. In situ ETEM observations were performed on a FEI Titan 80–300 ETEM using a HAADF detector. The water vapour pressure was controlled at ~10^{-3} mbar by a lab-developed gas-delivery system. The sample was held in the controlled environment for 30 min at each measurement temperature; the electron beam was blanked during the heating intervals and was only opened instantaneously for imaging. Raman spectroscopy data were obtained on a Horiba Jobin-Yvon using a 532 nm laser and an integration time of 4 s (repeated four times). The surface area and pore size distribution were measured by a Tristar II 3020 gas-adsorption analyser (Micromeritics). The surface area and pore size distribution were measured by a Micromeritics ASAP 2020 Porosimeter Test Station (Micromeritics). The metal loading was performed by inductively coupled plasma mass spectroscopy (Thermo Scientific Element 2 ICP-MS) by first dissolving our samples in aqua regia and then diluting with 2% HCl.

The X-ray absorption spectroscopy measurement at the Pt L$_3$ edge (11,564 eV) was performed on the bending-magnet beamline of the X-ray Science Division (9-BM-B) at the Advanced Photon Source, Argonne National Laboratory. The radiation was monochromatized by a Si(111) double-crystal monochromator. Harmonic rejection was accomplished with a rhodium-coated flat mirror. The energy was calibrated with Pt foil at the Pt L$_3$ edge. All the spectra were collected in fluorescence mode by a four-element silicon drift detector (Vortex-ME4, SII NanoTechnology USA, Inc.). Standard procedures based on Athena and Artimas software were used to fit the X-ray absorption spectroscopy data. The EXAFS coordination parameters were obtained by a least-squares fit in k space of the k^3-weighted Fourier transform data from 3.0 to 12.0 Å^{-1}, and the first shell fit of the magnitude and imaginary parts were performed between 1.2 and 2.0 Å.

MD simulations. We used the large-scale atomic/molecular massively parallel simulator to perform MD simulations[42]. To consider the bond interactions between the Pt and C atoms, the ReaxFF potential was used to describe the interaction between atoms in the Pt/graphene system[41]. The simulation was performed on a canonical ensemble (NVT) using the Nosé–Hoover thermostat with a 0.25 fs time step. We first equilibrated the Pt/graphene system at 300 K for 2.5 ps. Then, we performed repeated heating to 1,500 K for 25 ps and cooling to 300 K for 12.5 ps for a total of 50 times (which mimics the shockwave process). Finally, we slowly increased the temperature of the system to 1,500 K for 100 ps after the single Pt atoms formed to observe the stability of these atoms on the graphene sheet (which

mimics the thermal annealing process). In the simulation, the graphene sheet was 10 nm × 10 nm in size, and the defects were created by removing C atoms randomly. Also, 80 Pt atoms on the graphene sheet were located randomly. The binding energy of the Pt atom to graphene was defined as:

$$E_b = E_{Pt/graphene} - E_{Pt} - E_{graphene} \tag{1}$$

in which $E_{Pt/graphene}$, E_{Pt} and $E_{graphene}$ are the average potential energies of the Pt/graphene system, isolated Pt atom and graphene sheet with a fixed geometry, respectively. Under this definition, a more-negative binding energy indicates a stronger interaction between the graphene and Pt. Before calculating the potential energies, the energy of the system was first minimized using the conjugate gradient algorithm until either the total energy change between successive iterations divided by the energy magnitude was less than or equal to 10^{-6} or the total force was less than 10^{-6} eV Å^{-1}.

The reaction energy barrier was calculated by:

$$\Delta E = E_{final} - E_{initial} \tag{2}$$

in which E_{final} and $E_{initial}$ are the potential energies of the corresponding initial state and final state, respectively. $\Delta E > 0$ means the reaction is an endothermic reaction (not thermodynamically favourable) and $\Delta E < 0$ indicates that the reaction is an exothermic process and is thermodynamically favourable.

DFT simulations. DFT implemented in the Vienna ab initio simulation package[38,40] was performed to determine the atomic interaction between platinum and graphene. The generalized gradient approximation of the Perdew–Burke–Ernzerhof functional[39] was used for exchange and correlation interaction. The Brillouin zone was sampled by a 2 × 2 × 1 Monkhorst and Pack[37] grid. The cutoff energy in our calculation was 400 eV. All the calculations were relaxed to minimize the total energy of the system until the atomic forces converged to 0.01 eV Å^{-1}. Period boundary conditions were applied in both in-plane and interlayer directions. To eliminate the interaction between periodic images of atoms, a 12.75 Å × 12.49 Å cubic supercell was used to investigate the interaction of Pt atoms with graphene and a vacuum space of 15 Å perpendicular to the graphene plane. Given the existence of a suspending bond, all our calculations were added the spin polarization. For single-atom dispersion on C_3N_4 and TiO_2, the simulation (boundary and convergent conditions) was set using similar but adaptive rules.

Catalytic studies. Catalytic CO conversion was conducted in a fixed-bed flow reactor at atmospheric pressure. Typically, 15 mg of catalyst (Pt HT-SAs on CA-CNFs) was loaded into a quartz tube reactor (7 mm inner diameter). Prior to the reaction, the catalyst was pretreated in He (50 ml min^{-1}) for 2 h, and then cooled to 50 °C. At 50 °C, the gas flow was switched to the reactant gas feed (50 ml min^{-1}), which contained 1% CO and 4% O_2, balanced by He. The reaction was then carried out at various temperatures, which were increased stepwise from 50 °C to 300 °C. We allowed the system to reach a steady state before product analysis. To determine the conversion of the reactants and the product yields, a Fourier transform infrared spectrometer (Nicolet 6700, Thermo Scientific) equipped with a long path (5 m) gas cell and an mercury–cadmium–telluride detector (with a resolution of 8 cm^{-1}) was used to analyse CO (2,173 cm^{-1}). The kinetic measurements were carried out below 200 °C and with gas hourly space velocity of 400 l g$_{cat}^{-1}$ h^{-1} to ensure that the reaction condition was within the kinetic zone. The long-term stability test was measured at 220 °C.

The catalytic non-oxidative conversion of CH_4 was conducted in a fixed-bed flow reactor at atmospheric pressure. Before the reaction, a pretreatment was applied: 50 mg of catalyst (Pt HT-SAs on an ALD CA-CNF) (40–60 mesh) was loaded into a microflow quartz reactor (7 mm inner diameter), heated to 110 °C at a rate of 5 °C min^{-1} under He (50 ml min^{-1}) and held at 110 °C for 1 h. After pretreatment, the temperature was increased to 700 °C under He and the gas flow was then switched to 90% CH_4/He (20 ml min^{-1}, space velocity = 241 g$_{cat}^{-1}$ h^{-1}). The reaction temperature was kept at 700 °C and the reaction was run for 20 h. To determine the conversion of the reactants and the formation of products, a gas chromatograph (GC-2010 plus, Shimadzu) equipped with a SH-Rt-Q-BOND column and a BID detector were employed. All the lines between the reactor outlet and gas chromatograph sampling loop inlet were heat traced to 90 °C to prevent product condensation. The methane conversion, hydrocarbon product selectivity and coke deposition selectivity were calculated according to the mass balance.

Data availability

The data that support the plots within this paper and other findings of this study are available from the corresponding authors upon reasonable request.

References

45. Marcano, D. et al. Improved synthesis of graphene oxide. *ACS Nano* **4**, 4806–4814 (2010).
46. Jacob, R. J., Kline, D. J. & Zachariah, M. R. High speed 2-dimensional temperature measurements of nanothermite composites: probing thermal vs. gas generation effects. *J. Appl. Phys.* **123**, 115902 (2018).